
Measurement noise scaling laws for cellular representation learning

Gokul Gowri^{1,2} Peng Yin^{1,2} Allon Klein²

Abstract

Deep learning scaling laws predict how performance improves with increased model and dataset size. Here we identify measurement noise in data as another performance scaling axis, governed by a distinct logarithmic law. We focus on representation learning models of biological single cell genomic data, where a dominant source of measurement noise is due to molecular undersampling. We introduce an information-theoretic metric for cellular representation model quality, and find that it scales with sampling depth. A single quantitative relationship holds across several model types and across several datasets. We show that the analytical form of this relationship can be derived from a simple Gaussian noise model, which in turn provides an intuitive interpretation for the scaling law. Finally, we show that the same relationship emerges in image classification models with respect to two types of imaging noise, suggesting that measurement noise scaling may be a general phenomenon. Scaling with noise can serve as a guide in generating and curating data for deep learning models, particularly in fields where measurement quality can vary dramatically between datasets.

1. Introduction

Scaling laws in machine learning describe how model performance improves with increases in key resources like data, compute, and model parameters, often following power-law relationships (Hestness et al., 2017; Rosenfeld et al., 2019; Kaplan et al., 2020; Bahri et al., 2024). These empirical relationships have become crucial for understanding the fundamental limits of neural networks and for making principled decisions about resource allocation in training large models (Hoffmann et al., 2022). Another axis in which

model performance can vary is the noise in training data. But less is known about the effect of measurement noise on performance scalability. Prior work has studied the effects of dataset balance or data pruning on model scaling (Sorscher et al., 2022; Fournier et al., 2024; Covert et al., 2024), and model robustness to noise has also been evaluated in specific domains (Dodge & Karam, 2016; Chen et al., 2019; Bansal et al., 2022). We ask here whether there is evidence of a quantitative scaling relationship between dataset noise and model performance.

Our motivation is in considering representation learning in the biological sciences, and particularly single cell genomic measurements such as single cell RNA sequencing (scRNA-seq). These measurements provide intricate yet noisy and incomplete views of cellular states (Gunawan et al., 2023). A critical step toward using such measurements to model cellular behavior is representing data in a way that preserves biological signal while regressing out technical noise. Many computational approaches have been proposed to represent single-cell data. Beyond linear methods, the most widely used approach has been representation learning by dimensionality reducing models such as variational autoencoders (VAEs) (Kingma & Welling, 2013; Lopez et al., 2018). There has been significant recent interest in using massive collections of single cell data to learn more generalizable, and ultimately universal, representations of cellular measurements (Bunne et al., 2024). For these problems of increasing scale, a wide variety of modeling approaches have been explored, including transformer-based architectures (Theodoris et al., 2023; Cui et al., 2024; Heimberg et al., 2024; Richter et al., 2024).

Puzzlingly, initial attempts to learn representations from large single cell transcriptomic datasets have not clearly revealed the benefits of scale. For several tasks, including batch integration, cell type annotation, and perturbation response prediction, representations learned from $> 10^7$ cells do not significantly outperform simple linear baselines (Kedzierska et al., 2023; Boiarsky et al., 2023; Ahlmann-Eltze et al., 2024). Furthermore, it has been empirically observed that increasing the number of training cells beyond 10^5 often do not improve representations with respect to cell type annotation or batch correction performance (DenAdel et al., 2024).

¹Wyss Institute for Biologically Inspired Engineering
²Department of Systems Biology, Harvard University. Correspondence to: Gokul Gowri <ggowri@g.harvard.edu>, Allon Klein <allon_klein@hms.harvard.edu>.

In this work, we explore the possibility that poor scaling behavior is related to measurement noise in single cell transcriptomics. While modern transcriptomic techniques are powerful, accurately quantifying transcript abundance in a single cell is fundamentally challenging due to the low numbers of molecules per cell. Though sensitivity is increasing with ongoing technology development (Hagemann-Jensen et al., 2020), for many existing technologies the molecular capture efficiency is significantly below 50%, and in some cases capture rate is further decreased by insufficient sequence depth (Svensson et al., 2017). As a result, measured transcript counts are subject to undersampling noise.

The effect of transcript undersampling has been relatively well studied from the perspective of trade-offs between number of cells in an experiment and sensitivity of measurements, as it is often a practical consideration for resource allocation (Kim et al., 2024; Moriel et al., 2024; Svensson et al., 2019). However, the effect of transcript undersampling on deep learning models and their scalability is not well understood.

Here, we introduce an information-theoretic framework for studying the scalability of representation learning models with respect to changes in measurement noise and dataset size. We use this framework to study popular cellular representation learning approaches. For all evaluated model types and datasets, we find a consistent empirical scaling law with respect to transcripts per cell. We show that the form of this scaling law can be derived by analogy to additive Gaussian noise channels, and that the resulting theoretical framework can be used to guide experimental design. Finally, we show that measurement sensitivity scaling laws generalize beyond single cell transcriptomics by studying the effect of multiple types of imaging noise on visual representation learning.

2. Approach

We are interested in studying and comparing the scalability of representation learning models across data, subjected to different levels of measurement noise. In this section we introduce (1) a metric for representation quality; (2) the choice of datasets and models evaluated; and (3) our approach to scaling analysis.

An information-theoretic probing metric of representation quality. To quantify representation quality one might consider using a particular loss function, but any such choice would be specific to a model type and data distribution (Brandfonbrener et al., 2024). Instead, our proxy for representation quality will be the information that a representation contains about an external signal.

This approach is related to linear probing, which can be seen as estimating mutual information between a represen-

tation and a classification label (Belinkov, 2022; Pimentel et al., 2020). Here, we generalize the idea of probing beyond linear classification. We directly estimate the mutual information between representations and auxiliary signals which can be high-dimensional and continuous. We refer to this as *information-theoretic probing*. Formally, for a source variable X , auxiliary signal Y , and Z a noisy measurement of X , we define the quality of a representation function f as the estimated mutual information $I(f(Z); Y)$. We are interested in how $I(f(Z); Y)$ scales as a function of the noisiness of Z and the number of samples used to fit f .

Estimating mutual information is nontrivial, especially in high dimensions. To do so, we will use a recently developed neural-network based technique which enables close approximation of mutual information in high dimensions (Gowri et al., 2024). To allow consistent comparisons between different representations, in all experimental settings we learn representations on a subset of the data and then estimate mutual information using a different subset. The subset used to estimate mutual information remain fixed across models, such that differences between measured mutual information is the result of differences between representations rather than sampling artifacts. Details of mutual information estimation are given in Appendix A.3.

Datasets and models. We consider four types of X, Y pairs in the field of cellular representation learning. We use single-cell transcriptomic measurements with paired measurements such that in all cases, X is a single-cell transcriptional profile. We use the transcriptome data to learn the representations, and then estimate mutual information between representations and auxiliary signals. The four corresponding Y are:

1. **Granular cell type labels**, using a dataset of peripheral blood mononuclear cells (PBMCs) annotated using a paired antibody panel through CITE-seq (Hao et al., 2021).
2. **Surface protein abundances** of PBMCs measured by an antibody panel through CITE-seq (Hao et al., 2021).
3. **Transcriptional profile of a clonally related cell** in mouse hematopoietic stem cells measured using lineage-traced scRNA-seq (Weinreb et al., 2020).
4. **Transcriptional profile of a spatially adjacent cell** in a coronal mouse brain section measured using MER-FISH (Vizgen, 2021).

We evaluate the scalability of representations learned in each of these four datasets using (1) the VAE-based scVI (Lopez et al., 2018), (2) a minimal reimplement of the transformer-based Geneformer (Theodoris et al., 2023)

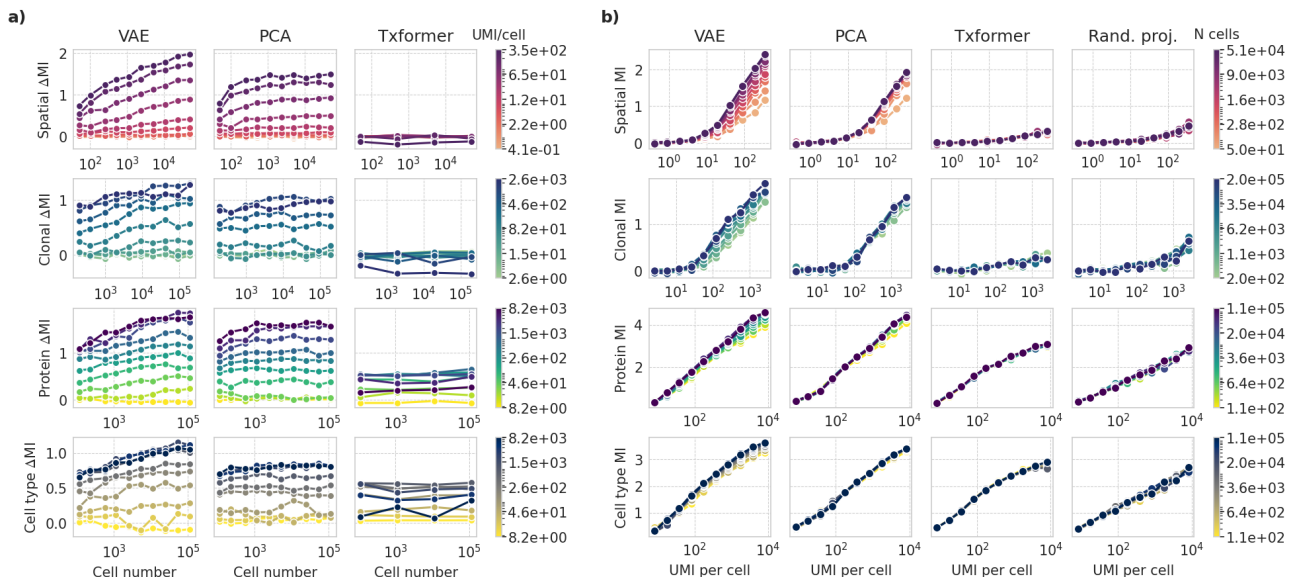


Figure 1: *Measurement sensitivity and dataset size scaling experiments.* *a)* Information gained above random projection (denoted ΔMI) for models trained on various datasets, shown as a function of training dataset size (cell number, \log_{10} scale), *b)* Representation information as a function of UMI per cell (\log_{10} scale) for all tested models and datasets, including random projection.

which we call Txformer (Appendix A.4), and linear baselines of (3) PCA and (4) random projection. The scVI, PCA, and random projection representations are 16-dimensional, and the Txformer representations are 128-dimensional.

While we include results for all models, we will focus the majority of our discussion on PCA and VAE representations. This is because Txformer does not exhibit any clear dataset size scaling – a result that is in line with a recent benchmarking study of transformer-based models trained on scRNA-seq data (DenAdel et al., 2024). In Appendix A.5, we show that the poor performance of our Txformer is not the result of details particular to our implementation: Txformer representations are roughly as informative as Geneformer representations (Appendix Figure 9). Instead, we identify two contributors to poor performance: (1) information loss during rank-based tokenization (Appendix Figure 12), and (2) lack of a clear relationship between mean-pooled cell embedding quality and masked language modeling loss (Appendix Figure 13).

In Section 6, we then additionally consider X, Y pairs of images and image labels from the Caltech101 image dataset (Fei-Fei et al., 2004), and consider the scalability of MobileNetv2 image classifiers with respect to measurement noise (Sandler et al., 2018).

Preprocessing details for all datasets can be found in Appendix A.2, and all model implementation details are given

in Appendix A.4.

Approach to scaling analysis To study the scalability of cellular representation learning models with respect to measurement noise, we simulate increasing measurement noise by binomially downsampling measured transcript counts – also referred to as unique molecular identifiers (UMIs) – in each of the four datasets, in line with prior work (Ahlmann-Eltze & Huber, 2023). And, following classic analyses revealing scaling laws in deep learning (Hestness et al., 2017), we randomly subsample training data points to achieve different dataset sizes.

3. Scaling laws for cellular representations

Figure 1 introduces the analyses of model performance as a function of count-downsampling noise and cell number. Random projections, which are not a function of training data, do not improve with increasing training dataset size. For VAE and PCA representations, Fig. 1a shows that representation quality exceeds that of random projection as would be expected, and that quality increases and then plateaus with dataset size, generally following a scaling behavior that agrees with a saturating power-law of the form

$$I(N) = I_{\infty} - \left(\frac{N}{N_0}\right)^{-s} \quad (1)$$

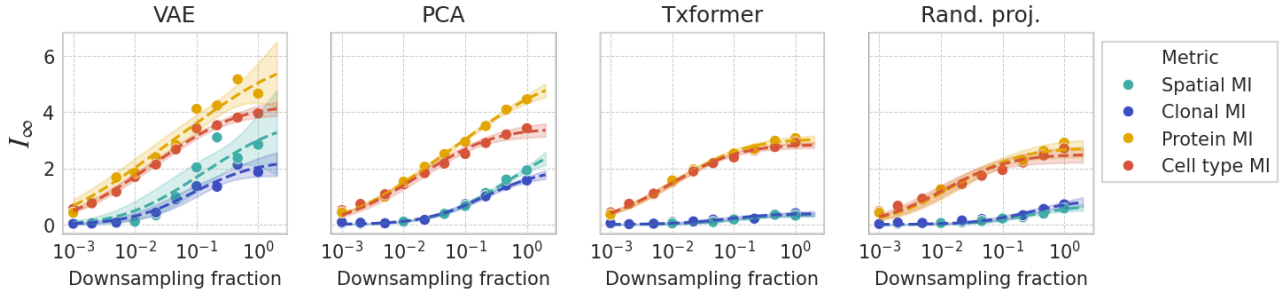


Figure 2: *Estimated I_∞ values for models across UMI downsampling conditions.* Each scatterplot point corresponds to an I_∞ estimate from Eq. 1. Dotted line denotes Eq. 2 fit to the estimated I_∞ . Shaded region denotes 2σ confidence interval. Downsampling fraction refers to fraction of total counts preserved from original dataset.

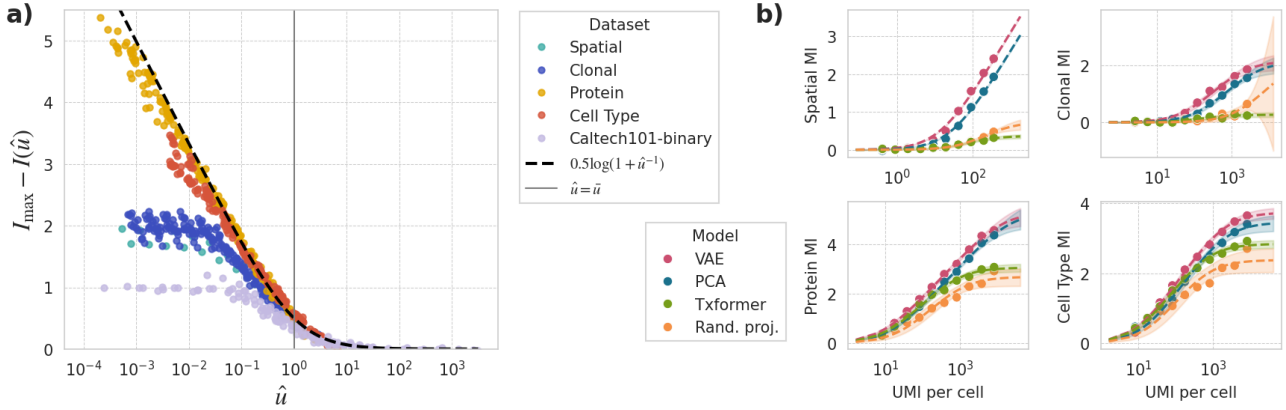


Figure 3: *Experimental data collapses on to scaling curves.* *a)* Each scatterplot point corresponds to an empirically measured representation information for a PCA, VAE, or MobileNetv2 model trained on data of varying quality, with values rescaled to lie on nondimensionalized axes. Dotted line corresponds to Eq. 6. Models for which \mathcal{I}_{\max} estimates are poorly constrained are omitted. *(b)* Example fits of Eq. 2 for cellular representation learning models trained on full dataset size. Shaded region denotes 2σ confidence intervals. Individual fits for each dataset size are given in Appendix Fig. 15.

where N is the number of training data points, and N_0 , s , I_∞ are parameters fit to observations (Fig. 2, Appendix Fig. 14). This form is consistent with model loss scaling behavior observed in several settings (Kaplan et al., 2020). However, one can observe in Fig. 2 that the parameter values vary with the degree of measurement noise (UMIs per cell).

We find that for fixed dataset size, model performance scales in a remarkably consistent way with the measurement noise, following a noise-scaling relationship:

$$\mathcal{I}(u) = \mathcal{I}_{\max} - \frac{1}{2} \log \frac{1 + u/\bar{u}}{u/\bar{u} + 2^{-2\mathcal{I}_{\max}}} \quad (2)$$

where u represents the number of UMIs per cell, \mathcal{I}_{\max} is the maximal information that can be extracted from a noiseless

measurement at a fixed sample size, and \bar{u} establishes noise scale (e.g. the number of UMIs per cell at which a model with $\mathcal{I}_{\max} \gg 1$ loses 1/2 a bit of information due to noise). This scaling behavior can be seen in the aforementioned variation of estimated I_∞ (from Eq. 1) shown in Fig. 2, as well as in Fig. 3a, where appropriate axis rescaling leads to a collapse of the complete performance curves from all models and datasets onto a single asymptotic form of Eq. 2 (varying only at $u \rightarrow 0$), and Fig. 3b, where noise-scaling behavior of cellular representation learning models is closely approximated by Eq. 2. The existence of this noise scaling relationship in biological representation learning represents the central result of this paper. The remainder of this paper studies the origin of the particular relationship identified here, discusses several of its practical implications, and shows that it appears to generalize beyond biological data.

4. A simple model of noise scaling

4.1. Model definition and analytical results

The mathematical form of noise-scaling in Eq. 2 can be derived from a simple model, which also then offers an interpretation for the underlying scaling parameters. Let X, Y be multivariate Gaussian random vectors representing signals distributed as follows

$$\begin{aligned} Y &\sim \mathcal{N}(1, \Sigma_Y) \\ X &= Y + U \end{aligned}$$

where $U \sim \mathcal{N}(0, \Sigma_U)$.

Next, let Z be a random vector representing a noisy measurement of X with signal-to-noise ratio α :

$$Z = \alpha X + \mathcal{N}(0, I_n)$$

In our empirical results for transcriptomic data, X corresponds to the true transcript counts, Y corresponds to an auxiliary signal, and Z corresponds to the representation extracted from a noisy measurement of X . We are interested in how $I(Y; Z)$ scales as a function of α . The relationship between α and $I(Y; Z)$ is specified by the following theorem.

Theorem 4.1. *For the three variable Gaussian noise model specified above,*

$$I(Y; Z) = \frac{1}{2} \log \frac{\det(\Sigma_Y + \Sigma_U + \alpha^{-2} I_n)}{\det(\Sigma_U + \alpha^{-2} I_n)} \quad (3)$$

In the special case where $n = 1$:

$$I(Y; Z) = \frac{1}{2} \log \frac{\alpha^2(\sigma_Y^2 + \sigma_U^2) + 1}{1 + \sigma_U^2 \alpha^2} \quad (4)$$

where $\Sigma_Y = \sigma_Y^2, \Sigma_U = \sigma_U^2$.

This theorem follows directly from a textbook result for Gaussian vector noise channels (Guo, 2004; Polyanskiy & Wu, 2024) (proof in Appendix A.1).

We can nondimensionalize this functional form to identify two interpretable characteristic parameters which define scaling behavior. First, we can note that

$$\begin{aligned} \mathcal{I}_{\max} &= \lim_{\alpha \rightarrow \infty} I(Y; Z) = I(X; Y) \\ &= \frac{\sigma_Y^2 + \sigma_U^2}{\sigma_U^2}. \end{aligned}$$

Then, by defining $\bar{u} = 1/\sigma_U^2$ and $\hat{u} = \alpha^2/\bar{u}$, we observe that Eq. 4 fully recovers the form of the empirical noise-scaling law in Eq. 2.

To make contact with our experimental setting of cellular representations, we need to relate the measurement noise – in terms of the number of UMI (mRNA transcripts) counts sampled per cell – to the explicit signal-to-noise ratio α . To do so, we note that the noise in discrete transcriptomic count data is Poisson in nature, with a coefficient of variation that scales as $\propto \text{UMI}^{-1/2}$ (Klein et al., 2015). It is therefore sensible to approximate $\alpha^2 = \text{CV}^{-2} = \kappa \cdot \text{UMI}$ for some positive constant κ . With this approximation, we can apply Eq. 2 to transcriptomic data by defining $\hat{u} = \text{UMI}/\bar{u}$ and absorbing the constant κ in our definition $\bar{u} = (\kappa\sigma_U^2)^{-1}$. Similar approximate relationships between α and data quality metrics can be derived for other notions of measurement noise, as we will show in our scaling analysis with image data (Section 6).

4.2. Data collapse onto scaling curves

When $\hat{u} \gg 2^{-2\mathcal{I}_{\max}}$, either because \mathcal{I}_{\max} is large or the effective signal-to-noise ratio (number of UMIs per cell) is high, we have that

$$\mathcal{I}(\hat{u}) \approx \mathcal{I}_{\max} - \frac{1}{2} \log \frac{1 + \hat{u}}{\hat{u}} \quad (5)$$

If the toy model faithfully captures observed scaling behavior, then in the regime where $\hat{u} \gg 2^{-2\mathcal{I}_{\max}}$ our experimentally measured data points (when appropriately rescaled) should collapse onto the one-dimensional manifold defined by

$$\mathcal{I}_{\max} - \mathcal{I}(\hat{u}) \approx \frac{1}{2} \log \frac{1 + \hat{u}}{\hat{u}} \quad (6)$$

And indeed, we find this is the case (Fig. 3). When the number of UMIs is sufficiently large such that the approximation is close (right side of plot), we see that all experimentally measured data points collapse onto Eq. 6. When the number of UMIs is small and the approximation does not hold (left side of plot), we see divergence from the asymptotic form. The point of divergence is stratified by dataset, which is expected as each dataset will have different regime where $\hat{u} \approx 2^{-2\mathcal{I}_{\max}}$.

5. Practical implications for cellular representation learning

We next consider the practical implications of measurement noise scaling for cellular representation learning. In the next section, we will pose and answer questions relating to up-scaling potential of the models considered, model selection, and the noise sensitivity of different learning tasks.

5.1. Are existing measurements sensitive enough to saturate model performance?

From Eqs. 1 and 2 we can project the benefit of upscaling: increasing cell number, or UMIs per cell, for each of the learning tasks evaluated. The results (tabulated in Tables 1, 2) show that the projected gains for increasing measurement sensitivity are substantial, while expected benefits of further scaling the size of the cell datasets evaluated in this study would be modest, with no projected gain beyond 0.2 bits. By contrast, the projected gain from increasing measurement sensitivity ranges from 0.13 to 1.64 bits of information. The lowest gain is for cell type information, which is in line with the fact that it is the least complex of the auxiliary signals tested. Thus, the existing measurements are sensitive enough to saturate representation quality with respect to cell type classification. In contrast, for VAE and PCA representations we can project a gain of over 1.5 bits of information by increasing MERFISH sensitivity by an order of magnitude. This is in line with the fact that MERFISH typically captures roughly an order of magnitude fewer transcripts per cell than most droplet-based scRNA-seq methods.

Table 1: *Projected information gained (in bits) from increasing dataset size by a factor of 10.* Random projection and Txformer are omitted as they do not appreciably scale with dataset size.

	Clonal	Spatial	Protein	Cell type
VAE	0.01	0.16	0.04	0.07
PCA	0.06	0.00	0.00	0.00

Table 2: *Projected benefit of increasing measurement sensitivity (mean UMIs per cell) by an order of magnitude for each dataset and modelling approach.*

	Clonal	Spatial	Protein	Cell type
VAE	0.27	1.64	0.57	0.13
PCA	0.46	1.61	0.73	0.13
Txformer	0.01	0.06	0.06	0.04
Rand. Proj.	–	0.23	0.07	0.04

5.2. Which modeling approach will be most effective on more sensitive measurements?

Across the tasks and approaches considered here, we project that VAEs will be the most effective model type on more sensitive measurements. For the limiting case of perfectly noiseless measurements, the parameter \mathcal{I}_{\max} directly tells us the projected performance. In Table 3, we tabulate \mathcal{I}_{\max} for each considered model type and dataset. In all cases where \mathcal{I}_{\max} can be estimated, VAE representations have the highest estimated value. It is interesting to note that PCA

matches or nearly matches the \mathcal{I}_{\max} of VAEs for clonal and protein information metrics, suggesting that the underlying structure of these datasets is largely linear in the absence of measurement noise.

Table 3: *Estimated \mathcal{I}_{\max} values for various models and datasets.* Dashes indicate poorly constrained parameter estimates.

	Clonal	Spatial	Protein	Cell type
VAE	2.17	–	5.29	3.73
PCA	2.15	–	5.29	3.45
Txformer	0.27	0.38	3.06	2.84
Rand. Proj.	–	0.74	2.68	2.38

5.3. How much task-relevant information has been lost to measurement noise?

Using \mathcal{I}_{\max} , we can also determine the amount of information lost to measurement noise for a given number of UMIs per cell. After rescaling, Eq. (2) can be equally rewritten as,

$$\mathcal{I}_{\text{lost}}(\hat{u}) = \frac{1}{2} \log \frac{1 + \hat{u}}{\hat{u} + 2^{-2\mathcal{I}_{\max}}} \quad (7)$$

This is of practical relevance as a type of data quality metric which considers the downstream consequence of measurement sensitivity, as opposed to an absolute molecular capture rate which is agnostic to the sensitivity necessary for a given task. We tabulate the $\mathcal{I}_{\text{lost}}$ for each dataset and modelling approach in Table 4. The $\mathcal{I}_{\text{lost}}$ for cell type annotation is < 0.15 bits for all models, again suggesting that cell type information in PBMCs is relatively saturated with respect to measurement noise.

Table 4: *Bits of information lost to measurement noise ($\mathcal{I}_{\text{lost}}$) for each dataset and modeling approach.* Dashes indicate poorly constrained parameter estimates.

	Clonal	Spatial	Protein	Cell type
VAE	0.30	–	0.67	0.14
PCA	0.54	–	0.89	0.14
Txformer	0.02	0.06	0.06	0.05
Rand. Proj.	–	0.28	0.08	0.04

5.4. How much measurement noise can be tolerated to achieve a certain representation quality?

Measurement noise scaling laws can be used to determine the sensitivity necessary to obtain a model with a specified amount of information. The fit parameter \bar{u} immediately tells us (up to rescaling) the measurement sensitivity necessary to reach $\frac{1}{2}$ bits below \mathcal{I}_{\max} . For a more general

relationship, we can easily invert Eq. 2 to obtain a function which estimates the necessary mean UMIs per cell necessary to learn a representation with a given information content with respect to a specified external signal:

$$\text{UMI}(\mathcal{I}) = \bar{u} \frac{2^{2\mathcal{I}} - 1}{2^{2\mathcal{I}_{\max}} - 2^{2\mathcal{I}}} \quad (8)$$

Combining this with \mathcal{I}_{\max} allows us to determine the number of UMIs per cell required to saturate model informativity to a desired degree. In Table 5, we show the number of UMIs required to reach 90% \mathcal{I}_{\max} for each dataset and model type. In line with our previous results, we see that with VAE and PCA representations far fewer UMIs per cell are necessary to saturate cell type information when compared to other signals.

Table 5: *Estimated number of UMIs (in thousands) required to reach $0.9 \cdot \mathcal{I}_{\max}$ for each model and dataset. Note that \mathcal{I}_{\max} is different for each modeling approach, so a lower number does not necessarily mean a better model, but rather one that requires fewer UMIs to saturate.*

	Clonal	Spatial	Protein	Cell type
VAE	3.907	–	11.55	2.579
PCA	8.751	–	18.43	2.938
Txformer	1.453	0.672	1.423	1.103
Rand. Proj.	–	1.944	2.188	1.308

5.5. Will more sensitive measurements lead to models that scale better with cell number?

While our theoretical framework does not fully relate dataset size scaling laws and measurement noise scaling laws, it is empirically clear that there is a relationship between measurement noise and cell number scalability. As seen in Fig. 2, Eq. 2 describes how \mathcal{I}_{∞} changes as a function of measurement noise – demonstrating that more sensitive measurements will lead to a higher plateau with respect to dataset size scaling. Intuitively, we might expect that increasing measurement noise will also decrease the information gain rate. This intuition can be quantified by measuring the information gained per \log_{10} cells as a function of measurement noise (Fig. 4). For VAE and PCA representations, we find that a 10-fold decrease in UMIs per cell reduces the information gain rate per \log_{10} cells above random projection by up to 3.3 fold, with an average of 1.8 fold. Cell type information gain rates remain similar for lower quality data, again suggesting the task of cell type annotation may not benefit from more sensitive measurements. Overall, these results indicate that the dataset size scalability of cellular representation learning models can be increased by training on more sensitively measured data.

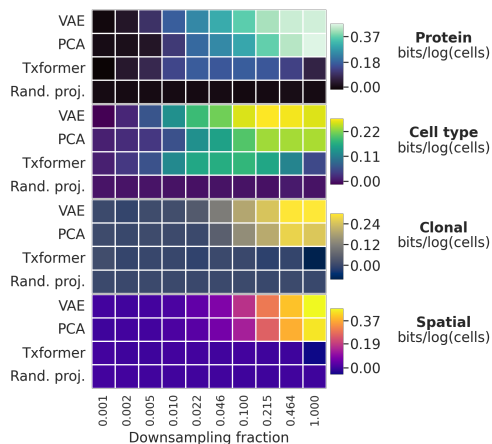


Figure 4: *Models extract information more slowly from noisier data. Each heatmap shows the mean information gained per \log_{10} cells in one dataset for each model type. Downsampling fraction corresponds to the fraction of the measured mean UMIs per cell which are included in the artificially undersampled dataset.*

6. Generalizing to other domains

While we have thus far studied measurement noise scaling laws as a phenomenon in single cell representation learning, the model and underlying principles presented in Section 3 are quite general, and may apply widely across domains. As a first step toward understanding their generality, we next ask if measurement noise scaling laws can accurately describe the behavior of image classification models under two types of imaging noise.

We study the behavior of MobileNetv2 image classifiers (Sandler et al., 2018) on a 5-class subset of the Caltech101 dataset (Fei-Fei et al., 2004) which we subject to varying levels of artificial noise (data preprocessing, model architecture, and training details are provided in Appendix A.2, A.4). As a slight modification from our setup in Section 3, we treat predicted class labels as the learned representation and use the true labels as the auxiliary signal with respect to which we measure informativity.

We first study the effect of Gaussian noise on images. Gaussian noise is common in imaging measurements (da Costa et al., 2016), and also matches the form of the noise in our model from Section 4. Across datasets subject to varying levels of pixel-wise Gaussian noise, we measure the mutual information between true and predicted labels of held out samples on the 5-class problem, as well as each of the 5 possible one-against-all classification problems.

Rather than defining \hat{u} in Eq. 2 in terms of UMIs, we now have $\hat{u} = \kappa^2 / \sigma_N^2$ where σ_N is the standard deviation

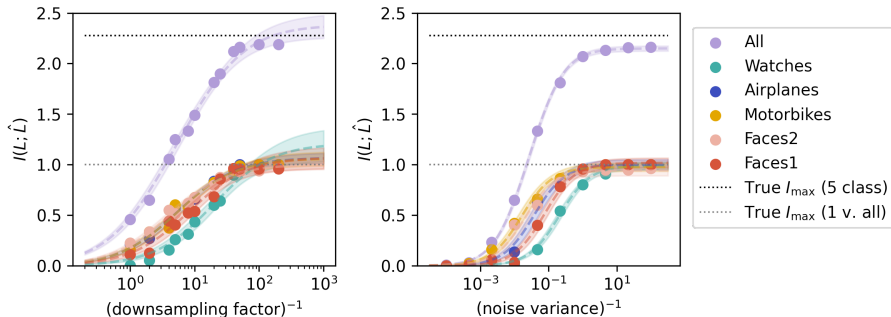


Figure 5: *Measurement noise scaling laws for image classifiers.* Mutual information between true and predicted labels for MobileNetv2 trained on datasets subject to varying levels of noise. (left) Effect of downsampling image resolution (i.e. pixelation). (right) Effect of i.i.d. pixel-wise Gaussian noise.

of the Gaussian noise. We find that for all classification problems, the scaling behavior with respect to Gaussian noise can be closely approximated by measurement noise scaling laws (Fig. 5). The saturation point of all functional approximations closely matches the theoretical maximum, which is the entropy of the true labels $H(L)$. While most of the one-against-all classification problems follow a similar scaling curve, we find that the performance of watch-against-all classification decays more quickly, indicating that this task requires higher data quality than other problems.

We next use a similar experimental setup to study the effect of decreasing image resolution (defined as pixel count). Here, rather than adding Gaussian noise, we average neighborhoods of pixels to decrease the effective resolution of an image. Here, we parameterize the scaling law with $\alpha = f^{-1}$ where f is the downsampling factor. Despite the fact that the structure of this noise is not Gaussian, we find that the measurement noise scaling laws still closely fit the observed scaling behavior (Fig. 5). And once again, we find that the watch-against-all classification problem is more sensitive to noise than other classes.

7. Discussion

It is certainly expected that noise in training data will affect model performance. But it is less clear whether there should be predictable rules by which performance degrades. In this paper, we showed that noise logarithmically degrades model performance in at least two distinct data types. We introduced an information-theoretic framework that recovers the empirically-observed noise-performance relationship, and used this framework to study noise-scaling. Evidence supporting the emergent relationship (Eq. 2) comes from 10^3 learned representations of three single cell transcriptomic datasets, and from image classification, suggesting that the relationship is likely general and may appear across other domains as well.

Our work suggests some practical guidelines for the development of cellular representation learning models. First, our empirical results show that Geneformer-like transformer models scale more poorly than VAE-based models and even linear dimensionality reduction. In line with some recent results (Kedzierska et al., 2023; Boiarsky et al., 2023; Ahlmann-Eltze et al., 2024), this suggests the inductive biases encoded by transformer architectures may not be well-suited for cellular representation learning. Second, our empirical results suggest that increasing the sensitivity (or molecular counts per cell) of existing high-throughput scRNA-seq technologies can have a significant impact on the performance of cellular representation learning models. There are several major efforts underway to collect datasets at the scale of billions of cells, and our results formally show the need to focus on data quality, even more so than on quantity alone.

Our work opens several possible threads of future study. First, the functional form derived in Section 4 has a simple form only for $n = 1$ dimensional variables. We found that this simple form still fits in high-dimensional settings. What are the properties of the high-dimensional problem that lead it to behave effectively one-dimensional? Second, our information-theoretic framework considers only measurement noise, and not the number of training samples. Ideally, we could use a similar framework to derive a joint scaling law over both dataset size and measurement noise.

One clear limitation of this work is that representation quality is defined with respect to external signals, such that the quality metric is tied to particular downstream uses. This was a deliberate choice, to ensure that quality had relevance to concrete tasks in cellular representation learning. An open question is if it is possible to construct information-theoretic representation quality metrics that do not rely on external signals. Such metrics would enable a more general analysis of self-supervised representation learning methods across a wider variety of datasets.

8. Broader impacts

The experiments (and pilot iterations) in this paper were performed on a single commercial GPU, and resulted in estimated 18.66 kg CO₂eq. Estimates made using (Lacoste et al., 2019).

Reproducibility The results of this paper can be reproduced by running the scripts provided in the repository at [this link](#).

9. Acknowledgements

We thank Jonathan Rosenfeld for formative discussions. This work is supported by funding from NIH Pioneer Award DP1GM133052, R01HG012926 to P.Y., and Molecular Robotics Initiative at the Wyss Institute. A.M.K. acknowledges support of an Edward Mallinckrodt Jr. Scholar Award.

References

- Ahlmann-Eltze, C. and Huber, W. Comparison of transformations for single-cell RNA-seq data. *Nat. Methods*, 20(5):665–672, 10 May 2023. ISSN 1548-7091,1548-7105. doi: 10.1038/s41592-023-01814-1.
- Ahlmann-Eltze, C., Huber, W., and Anders, S. Deep learning-based predictions of gene perturbation effects do not yet outperform simple linear methods. *bioRxiv*, pp. 2024.09.16.613342, 19 September 2024. doi: 10.1101/2024.09.16.613342.
- Bahri, Y., Dyer, E., Kaplan, J., Lee, J., and Sharma, U. Explaining neural scaling laws. *Proc. Natl. Acad. Sci. U. S. A.*, 121(27):e2311878121, 2 July 2024. ISSN 0027-8424,1091-6490. doi: 10.1073/pnas.2311878121.
- Bansal, Y., Ghorbani, B., Garg, A., Zhang, B., Krikun, M., Cherry, C., Neyshabur, B., and Firat, O. Data scaling laws in NMT: The effect of noise and architecture. *arXiv [cs.LG]*, 4 February 2022.
- Belinkov, Y. Probing classifiers: Promises, shortcomings, and advances. *Comput. Linguist. Assoc. Comput. Linguist.*, 48(1):207–219, 4 April 2022. ISSN 0891-2017,1530-9312. doi: 10.1162/coli_a_00422.
- Boiarsky, R., Singh, N., Buendia, A., Getz, G., and Sontag, D. A deep dive into single-cell RNA sequencing foundation models. *bioRxiv*, pp. 2023.10.19.563100, 23 October 2023. doi: 10.1101/2023.10.19.563100.
- Brandfonbrener, D., Anand, N., Vyas, N., Malach, E., and Kakade, S. Loss-to-loss prediction: Scaling laws for all datasets. *arXiv [cs.LG]*, 19 November 2024.
- Bunne, C., Roohani, Y., Rosen, Y., Gupta, A., Zhang, X., Roed, M., Alexandrov, T., AlQuraishi, M., Brennan, P., Burkhardt, D. B., Califano, A., Cool, J., Dernburg, A. F., Ewing, K., Fox, E. B., Haury, M., Herr, A. E., Horvitz, E., Hsu, P. D., Jain, V., Johnson, G. R., Kalil, T., Kelley, D. R., Kelley, S. O., Kreshuk, A., Mitchison, T., Otte, S., Shendure, J., Sofroniew, N. J., Theis, F., Theodoris, C. V., Upadhyayula, S., Valer, M., Wang, B., Xing, E., Yeung-Levy, S., Zitnik, M., Karaletsos, T., Regev, A., Lundberg, E., Leskovec, J., and Quake, S. R. How to build the virtual cell with artificial intelligence: Priorities and opportunities. *arXiv [q-bio.QM]*, 17 September 2024.
- Chen, P., Liao, B., Chen, G., and Zhang, S. Understanding and utilizing deep neural networks trained with noisy labels. *arXiv [cs.LG]*, 13 May 2019.
- Cover, T. M. and Thomas, J. A. *Elements of Information Theory*. Wiley & Sons, Incorporated, John, 2006. ISBN 9780471748823.
- Covert, I., Ji, W., Hashimoto, T., and Zou, J. Scaling laws for the value of individual data points in machine learning. *arXiv [cs.LG]*, 30 May 2024.
- Cui, H., Wang, C., Maan, H., Pang, K., Luo, F., Duan, N., and Wang, B. scGPT: toward building a foundation model for single-cell multi-omics using generative AI. *Nat. Methods*, 21(8):1470–1480, August 2024. ISSN 1548-7091,1548-7105. doi: 10.1038/s41592-024-02201-0.
- da Costa, G. B. P., Contato, W. A., Nazare, T. S., Neto, J. a. E. S. B., and Ponti, M. An empirical study on the effects of different types of noise in image classification tasks. *arXiv [cs.CV]*, 9 September 2016.
- DenAdel, A., Hughes, M., Thoutam, A., Gupta, A., Navia, A. W., Fusi, N., Raghavan, S., Winter, P. S., Amini, A. P., and Crawford, L. Evaluating the role of pre-training dataset size and diversity on single-cell foundation model performance. *bioRxiv*, pp. 2024.12.13.628448, 17 December 2024. doi: 10.1101/2024.12.13.628448.
- Dodge, S. and Karam, L. Understanding how image quality affects deep neural networks. In *2016 Eighth International Conference on Quality of Multimedia Experience (QoMEX)*, pp. 1–6. IEEE, June 2016. ISBN 9781509003549,9781509003532. doi: 10.1109/qomex.2016.7498955.
- Fei-Fei, L., Fergus, R., and Perona, P. Learning generative visual models from few training examples: An incremental bayesian approach tested on 101 object categories. pp. 178–178, 27 June 2004.
- Fournier, Q., Vernon, R. M., van der Sloot, A., Schulz, B., Chandar, S., and Langmead, C. J. Protein language models: Is scaling necessary? *bioRxiv*, pp.

- 2024.09.23.614603, 23 September 2024. doi: 10.1101/2024.09.23.614603.
- Gowri, G., Lun, X., Klein, A. M., and Yin, P. Approximating mutual information of high-dimensional variables using learned representations. In *The Thirty-eighth Annual Conference on Neural Information Processing Systems*, 6 November 2024.
- Gunawan, I., Vafaee, F., Meijering, E., and Lock, J. G. An introduction to representation learning for single-cell data analysis. *Cell Rep. Methods*, 3(8):100547, 28 August 2023. ISSN 2667-2375. doi: 10.1016/j.crmeth.2023.100547.
- Guo, D. *Gaussian channels: Information, estimation and multiuser detection*. PhD thesis, 2004.
- Hagemann-Jensen, M., Ziegenhain, C., Chen, P., Ramsköld, D., Hendriks, G.-J., Larsson, A. J. M., Faridani, O. R., and Sandberg, R. Single-cell RNA counting at allele and isoform resolution using Smart-seq3. *Nat. Biotechnol.*, 38(6):708–714, 4 June 2020. ISSN 1087-0156,1546-1696. doi: 10.1038/s41587-020-0497-0.
- Hao, Y., Hao, S., Andersen-Nissen, E., Mauck, 3rd, W. M., Zheng, S., Butler, A., Lee, M. J., Wilk, A. J., Darby, C., Zager, M., Hoffman, P., Stoeckius, M., Papalexi, E., Mimitou, E. P., Jain, J., Srivastava, A., Stuart, T., Fleming, L. M., Yeung, B., Rogers, A. J., McElrath, J. M., Blish, C. A., Gottardo, R., Smibert, P., and Satija, R. Integrated analysis of multimodal single-cell data. *Cell*, 184(13):3573–3587.e29, 24 June 2021. ISSN 0092-8674,1097-4172. doi: 10.1016/j.cell.2021.04.048.
- Heimberg, G., Kuo, T., DePianto, D. J., Salem, O., Heigl, T., Diamant, N., Scalia, G., Biancalani, T., Turley, S. J., Rock, J. R., Corrada Bravo, H., Kaminker, J., Vander Heiden, J. A., and Regev, A. A cell atlas foundation model for scalable search of similar human cells. *Nature*, pp. 1–3, 20 November 2024. ISSN 0028-0836,1476-4687. doi: 10.1038/s41586-024-08411-y.
- Helical. *helicalAI/helical*: v0.0.1a14, November 2024.
- Hestness, J., Narang, S., Ardalani, N., Diamos, G., Jun, H., Kianinejad, H., Patwary, M. M. A., Yang, Y., and Zhou, Y. Deep Learning Scaling is Predictable, Empirically. *arXiv [cs.LG]*, 1 December 2017.
- Hoffmann, J., Borgeaud, S., Mensch, A., Buchatskaya, E., Cai, T., Rutherford, E., Casas, D. d. L., Hendricks, L. A., Welbl, J., Clark, A., Hennigan, T., Noland, E., Millican, K., van den Driessche, G., Damoc, B., Guy, A., Osindero, S., Simonyan, K., Elsen, E., Rae, J. W., Vinyals, O., and Sifre, L. Training Compute-Optimal Large Language Models. *arXiv [cs.CL]*, 29 March 2022.
- Kaplan, J., McCandlish, S., Henighan, T., Brown, T. B., Chess, B., Child, R., Gray, S., Radford, A., Wu, J., and Amodei, D. Scaling laws for neural language models. *arXiv [cs.LG]*, 22 January 2020.
- Kedzierska, K. Z., Crawford, L., Amini, A. P., and Lu, A. X. Assessing the limits of zero-shot foundation models in single-cell biology. *bioRxiv*, pp. 2023.10.16.561085, 17 October 2023. doi: 10.1101/2023.10.16.561085.
- Kim, J., Kubal, S., and Schiebinger, G. Optimal sequencing depth for single-cell RNA-sequencing in Wasserstein space. *arXiv [math.ST]*, 22 September 2024.
- Kingma, D. P. and Welling, M. Auto-Encoding Variational Bayes. *arXiv [stat.ML]*, 20 December 2013.
- Klein, A. M., Mazutis, L., Akartuna, I., Tallapragada, N., Veres, A., Li, V., Peshkin, L., Weitz, D. A., and Kirschner, M. W. Droplet barcoding for single-cell transcriptomics applied to embryonic stem cells. *Cell*, 161(5):1187–1201, 21 May 2015. ISSN 0092-8674,1097-4172. doi: 10.1016/j.cell.2015.04.044.
- Lacoste, A., Luccioni, A., Schmidt, V., and Dandres, T. Quantifying the Carbon Emissions of Machine Learning. *arXiv [cs.CY]*, 21 October 2019.
- Lopez, R., Regier, J., Cole, M. B., Jordan, M. I., and Yosef, N. Deep generative modeling for single-cell transcriptomics. *Nat. Methods*, 15(12):1053–1058, December 2018. ISSN 1548-7091,1548-7105. doi: 10.1038/s41592-018-0229-2.
- Moriel, N., Memet, E., and Nitzan, M. Optimal sequencing budget allocation for trajectory reconstruction of single cells. *Bioinformatics*, 40(Suppl 1):i446–i452, 28 June 2024. ISSN 1367-4803,1367-4811. doi: 10.1093/bioinformatics/btae258.
- Paszke, A., Gross, S., Massa, F., Lerer, A., Bradbury, J., Chanan, G., Killeen, T., Lin, Z., Gimelshein, N., Antiga, L., Desmaison, A., Köpf, A., Yang, E., DeVito, Z., Raison, M., Tejani, A., Chilamkurthy, S., Steiner, B., Fang, L., Bai, J., and Chintala, S. PyTorch: An Imperative Style, High-Performance Deep Learning Library. *arXiv [cs.LG]*, 3 December 2019.
- Pedregosa, F., Varoquaux, G., Gramfort, A., Michel, V., Thirion, B., Grisel, O., Blondel, M., Prettenhofer, P., Weiss, R., Dubourg, V., Vanderplas, J., Passos, A., Cournapeau, D., Brucher, M., Perrot, M., and Duchesnay, E. Scikit-learn: Machine Learning in Python. *Journal of Machine Learning Research*, 12(85):2825–2830, 2011. ISSN 1533-7928.

- Pimentel, T., Valvoda, J., Maudslay, R. H., Zmigrod, R., Williams, A., and Cotterell, R. Information-theoretic probing for linguistic structure. *arXiv [cs.CL]*, 6 April 2020.
- Polyanskiy, Y. and Wu, Y. *Information theory: From coding to learning*. Cambridge university press, 2024.
- Richter, T., Bahrami, M., Xia, Y., Fischer, D. S., and Theis, F. J. Delineating the effective use of self-supervised learning in single-cell genomics. *Nat. Mach. Intell.*, pp. 1–11, 27 December 2024. ISSN 2522-5839,2522-5839. doi: 10.1038/s42256-024-00934-3.
- Rosenfeld, J. S., Rosenfeld, A., Belinkov, Y., and Shavit, N. A constructive prediction of the generalization error across scales. *arXiv [cs.LG]*, 27 September 2019.
- Sandler, M., Howard, A., Zhu, M., Zhmoginov, A., and Chen, L.-C. MobileNetV2: Inverted residuals and linear bottlenecks. *arXiv [cs.CV]*, 12 January 2018.
- Sorscher, B., Geirhos, R., Shekhar, S., Ganguli, S., and Morcos, A. S. Beyond neural scaling laws: beating power law scaling via data pruning. *Neural Inf Process Syst*, abs/2206.14486:19523–19536, 29 June 2022. doi: 10.48550/arXiv.2206.14486.
- Svensson, V., Natarajan, K. N., Ly, L.-H., Miragaia, R. J., Labalette, C., Macaulay, I. C., Cvejic, A., and Teichmann, S. A. Power analysis of single-cell RNA-sequencing experiments. *Nat. Methods*, 14(4):381–387, 6 April 2017. ISSN 1548-7091,1548-7105. doi: 10.1038/nmeth.4220.
- Svensson, V., da Veiga Beltrame, E., and Pachter, L. Quantifying the tradeoff between sequencing depth and cell number in single-cell RNA-seq. *bioRxiv*, pp. 762773, 9 September 2019. doi: 10.1101/762773.
- Theodoris, C. V., Xiao, L., Chopra, A., Chaffin, M. D., Al Sayed, Z. R., Hill, M. C., Mantineo, H., Brydon, E. M., Zeng, Z., Liu, X. S., and Ellinor, P. T. Transfer learning enables predictions in network biology. *Nature*, 618 (7965):616–624, 31 June 2023. ISSN 0028-0836,1476-4687. doi: 10.1038/s41586-023-06139-9.
- Virshup, I., Bredikhin, D., Heumos, L., Palla, G., Sturm, G., Gayoso, A., Kats, I., Koutrouli, M., Scverse Community, Berger, B., Pe’er, D., Regev, A., Teichmann, S. A., Finotello, F., Wolf, F. A., Yosef, N., Stegle, O., and Theis, F. J. The scverse project provides a computational ecosystem for single-cell omics data analysis. *Nat. Biotechnol.*, 41(5):604–606, May 2023. ISSN 1087-0156,1546-1696. doi: 10.1038/s41587-023-01733-8.
- Vizgen. Vizgen Data Release V1.0, May 2021. Title of the publication associated with this dataset: Mouse Brain Receptor Map.
- Weinreb, C., Rodriguez-Fraticelli, A., Camargo, F. D., and Klein, A. M. Lineage tracing on transcriptional landscapes links state to fate during differentiation. *Science*, 367(6479), 14 February 2020. ISSN 0036-8075,1095-9203. doi: 10.1126/science.aaw3381.

A. Appendix

In this appendix, we first prove our key theoretical result. Then, we summarize our data preprocessing methods. We then describe details of our mutual information estimates. Then, we provide implementation details for all model types studied in this work. Then, we interrogate the poor performance of Txformer, and compare its performance to zero-shot Geneformer (Theodoris et al., 2023) and scGPT (Cui et al., 2024). Finally, we provide additional visualizations to accompany main text results.

A.1. Analytical results for a toy model

Let X, Y be multivariate Gaussian random vectors representing signals distributed as follows

$$\begin{aligned} Y &\sim \mathcal{N}(1, \Sigma_Y) \\ X &= Y + U \end{aligned}$$

where $U \sim \mathcal{N}(0, \Sigma_U)$.

Next, let Z be a random vector representing a noisy measurement of X with signal-to-noise ratio α :

$$Z = \alpha X + \mathcal{N}(0, I_n)$$

In our empirical results for transcriptomic data, X corresponds to the true transcript counts, Y corresponds to an auxiliary signal, and Z corresponds to the representation extracted from a noisy measurement of X . We are interested in how $I(Y; Z)$ scales as a function of α . We next show that in the above toy model, the relationship between α and $I(Y; Z)$ can be exactly specified.

Theorem A.1 (Theorem 3.1). *For the three variable Gaussian noise model specified above,*

$$I(Y; Z) = \frac{1}{2} \log \frac{\det(\Sigma_Y + \Sigma_U + \alpha^{-2} I_n)}{\det(\Sigma_U + \alpha^{-2} I_n)} \quad (9)$$

In the special case where $n = 1$, denoting the variances σ_Y^2, σ_U^2 :

$$I(Y; Z) = \frac{1}{2} \log \frac{\alpha^2(\sigma_Y^2 + \sigma_U^2) + 1}{1 + \sigma_U^2 \alpha^2} \quad (10)$$

Proof. We will build on a basic result for Gaussian vector noise channels (Polyanskiy & Wu, 2024; Guo, 2004) which states that for independent Gaussian random vectors X, N ,

$$I(X; X + N) = \frac{1}{2} \log \frac{\det(\Sigma_X + \Sigma_N)}{\det(\Sigma_N)}$$

where Σ_X, Σ_N are the covariance matrices of X, N .

We will begin by rewriting Z in terms of Y . From definitions, we have

$$\begin{aligned} Z &= \alpha X + \mathcal{N}(0, I_n) \\ &= \alpha(Y + U) + \mathcal{N}(0, I_n) \\ &= \alpha(Y + \mathcal{N}(0, \Sigma_U)) + \mathcal{N}(0, I_n) \end{aligned}$$

Due to closure rules for Gaussians, we can rewrite

$$Z = \alpha Y + \mathcal{N}(0, \alpha^2 \Sigma_U + I_n)$$

Next, we observe that due to the scale invariance of mutual information (Cover & Thomas, 2006)

$$I(Y; Z) = I(Y; \alpha^{-1} Z)$$

$$\begin{aligned}
 &= I(Y; Y + \alpha^{-1}\mathcal{N}(0, \alpha^2\Sigma_U + I_n)) \\
 &= I(Y; Y + \mathcal{N}(0, \Sigma_U + \alpha^{-2}I_n))
 \end{aligned}$$

Now we can directly apply the Gaussian vector channel result:

$$\begin{aligned}
 I(Y; Z) &= I(Y; Y + \mathcal{N}(0, \Sigma_U + \alpha^{-2}I_n)) \\
 &= \frac{1}{2} \log \frac{\det(\Sigma_Y + \Sigma_U + \alpha^{-2}I_n)}{\det(\Sigma_U + \alpha^{-2}I_n)}
 \end{aligned}$$

And in the special case where $n = 1$, we have that

$$\begin{aligned}
 I(Y; Z) &= \frac{1}{2} \log \frac{\sigma_Y^2 + \sigma_U^2 + \alpha^{-2}}{\sigma_U^2 + \alpha^{-2}} \\
 &= \frac{1}{2} \log \frac{\alpha^2\sigma_Y^2 + \alpha^2\sigma_U^2 + 1}{1 + \sigma_U^2\alpha^2}
 \end{aligned}$$

□

A.2. Data preprocessing methods

In this section, we summarize key details of our data preprocessing methods. While the descriptions should be sufficient to reproduce our results, we also provide an annotated codebase in the supplemental files. First, we will describe our general data preprocessing pipeline applied to all single cell datasets, then we will describe dataset specific methods below. Finally, we will describe our image preprocessing pipeline.

For each dataset, transcript count downsampling, and cell number subsampling combination we implement a relatively standard Scanpy (Virshup et al., 2023) data processing pipeline. First, counts are uniformly randomly downsampled. Then counts are normalized cell-wise to a target sum of 10^4 counts per gene. Then they are log normalized, and genes with fewer than 3 counts in the dataset are removed. Then, if the dataset measures more than 750 genes, the top 750 highly variable genes are selected using the `seuratv3` algorithm. Finally, the cells are subsampled to a desired dataset size.

A.2.1. MERFISH MOUSE BRAIN DATASET FOR SPATIAL INFORMATION PROBING

We use the 67,821 single cell transcriptomes measured in coronal section 1 of replicate 1 in the Vizgen mouse brain data release (Vizgen, 2021). We remove “blank” measurements from the dataset, leaving 649 measurement dimensions. We define cell location by the center coordinate of the cell segmentation mask (which is provided in the metadata of the dataset). We construct a paired dataset of neighboring cells by randomly selecting one the 5 nearest cells as the neighbor pair for each cell in the dataset. Information probing then measures the information each cell representation contains about its neighbor pair.

A.2.2. LARRY HEMATOPIESIS DATASET FOR CLONAL INFORMATION PROBING

We pair clonally related cells as follows. In brief, we randomly pair clonally related cells between early and late timepoints. We first separate the dataset into cells profiled at early timepoints (day 2 and day 4), and final day 6 timepoint. Then, we subset the dataset for cells whose clonal barcodes appear in both early and late timepoints. Then, for each clone, we randomly select a cell from the early timepoint and pair it with a randomly selected cell from a late timepoint. Information probing then measures the information each cell representation contains about its clonally related pair.

A.2.3. CITE-SEQ PBMC DATASET FOR PROTEIN AND CELL TYPE PROBING

We use the CITE-seq PBMC dataset from (Hao et al., 2021) as distributed by `scvi-tools` (Virshup et al., 2023). For cell types, we use the `celltype.13` annotation, which contains 57 cell types.

A.2.4. CALTECH101

We use the Caltech101 (Fei-Fei et al., 2004) as distributed by Pytorch (Paszke et al., 2019). We rescale pixel intensity values to $[-1, 1]$, and crop images to 240×240 pixels. We then select the 5 classes with the largest number of images and subset only images from those 5 classes. This leaves a total of 2707 images. To downsample resolution by factor f , we tile the image in $240/f \times 240/f$ and each pixel is reassigned with the mean pixel value within its respective tile, in effect pixelating the image. To add Gaussian noise, we sample a 240×240 matrix i.i.d Gaussians with 0 mean and specified variance for each image and add it to the pixel values.

A.3. Mutual information estimation methods

All our information-theoretic probing of single cell representations involves high-dimensional variables. Estimating mutual information for high-dimensional variables is nontrivial due to the curse of dimensionality. We use a method called latent mutual information (LMI) approximation (Gowri et al., 2024) which embeds high-dimensional data in a low-dimensional space amenable for nonparametric MI estimation. For all LMI estimates in this paper, we use a latent space size of 32 dimensions (or 16 per variable). For cell type information probing, we convert discrete cell type labels into one-hot encoded vectors for MI estimation. In our Caltech101 experiments, we estimate MI directly between class labels. For this, we use a classical nonparametric estimator which is provided in the software implementation of (Gowri et al., 2024).

A.4. Model implementation details

Below we summarize the implementation details of the models we study in this work. While all details necessary for re-implementation are provided here, we also provide an annotated code base for reproducibility in the supplemental files. We provide also the training logs for differentiable models, which show that models do not have pathological training dynamics. For conciseness, we include only the models trained on PBMC scRNA-seq (used for cell type and protein information probing). The remaining training logs can be found in the supplemental files.

A.4.1. RANDOM PROJECTION IMPLEMENTATION

We randomly project our preprocessed count matrix of 750 genes to 16 dimensions with a 750×16 matrix populated with i.i.d standard unit variance Gaussian elements.

A.4.2. PCA IMPLEMENTATION

We compute principal components using the randomized SVD method implemented in `sklearn` (Pedregosa et al., 2011).

A.4.3. VAE IMPLEMENTATION

We use the `scvi` software package (Virshup et al., 2023). For each encoder and decoder, we use a single hidden layer with 512 units. We use a 16-dimensional latent space. We train with batch size of 512, and early stopping with patience of 45 epochs.

A.4.4. TXFORMER IMPLEMENTATION

Here we describe our model architecture, tokenization, and training details for Txformer, a lightweight reimplementation of Geneformer (Theodoris et al., 2023).

Tokenization Similar to the approach of Geneformer (Theodoris et al., 2023), we tokenize single cell transcriptomes through rank encoding. However, rather than using a gene vocabulary covering the whole genome, we instead restrict the vocabulary to the 750 selected HVGs for each dataset. For each gene, we first compute the median expression value among nonzero counts. We use these nonzero medians to normalize counts, then rank genes by normalized count in each cell. The tokenized cell is then the token correspond to each gene, ordered by rank. Genes with zero mean are dropped, and replaced by pad tokens.

Model architecture Txformer is an encoder-only model built using the Pytorch (Paszke et al., 2019) Transformer class, with the following parameters: 2 encoder layers, input window of 750 tokens, 128-dimensional embeddings, 4 attention heads, and 512-dimensional feed-forward networks. Layer norms use $\epsilon = 10^{-5}$. Positional encodings are learned parameters.

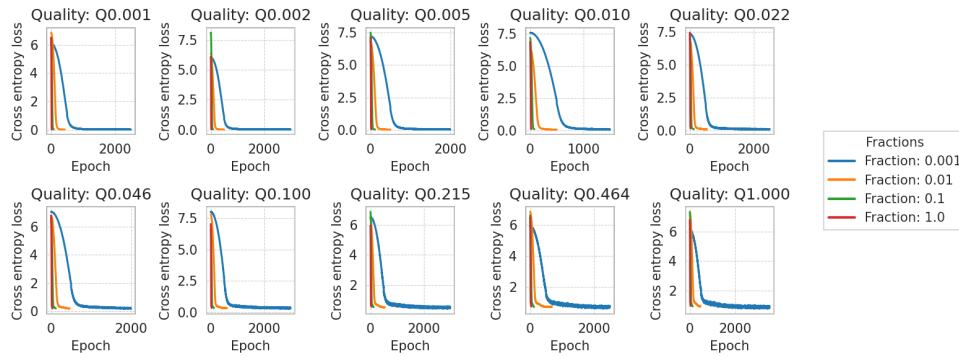


Figure 6: Txfomer training loss curves on downsampled and subsampled PBMC datasets. Quality refers to count downsampling, and fraction refers to cell number subsampling.

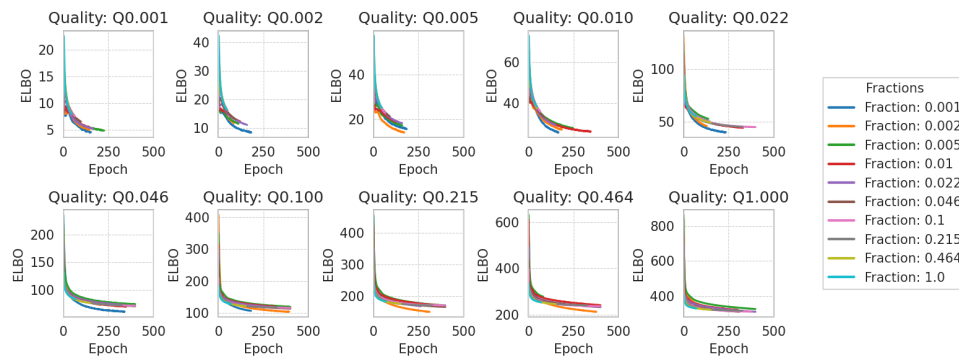


Figure 7: VAE training loss curves on downsampled and subsampled PBMC datasets. Quality refers to count downsampling, and fraction refers to cell number subsampling.

This is at a smaller scale than Geneformer’s 2048 token input size, 256-dimensional embeddings, and 6 encoder layers.

Training Data is first split into 80% train and 20% validation samples used to evaluate an early stopping criterion. We optimize a masked language modelling objective, where 15% of each input sequence is masked, and the cross-entropy loss is minimized for masked token reconstruction. We use a batch size of 32 samples. Validation loss is evaluated every 10^3 batches, and training is stopped when validation loss stops decreasing (i.e. with patience of 1). We choose this early stopping procedure to balance the amount of compute used to train models across differently sized datasets. Evaluating validation loss at the end of each epoch leads to models trained on small datasets having far fewer optimization steps. We optimize using Adam with a learning rate of 10^{-4} . A learning rate scheduler with a linear warmup followed by linear decay was implemented. The number of warmup steps was set to 10% of the total training steps. Training used a dropout rate of 0.1.

Cell embedding Cell embeddings are mean-pooled embeddings from the last transformer layer.

A.4.5. MOBILENETV2

We finetune the ImageNet pretrained MobileNetv2 architecture distributed with Pytorch (Paszke et al., 2019). To adapt it to our 5-class subset of Caltech101, the final classification layer is replaced with a fully connected layer with a 5-dim output. Then, with a 1 : 1 train-test split, we optimize a cross-entropy loss for 5 epochs, using Adam with a learning rate of 10^{-4} .

A.5. Diagnosing Txfomer performance

One of our empirical findings is that Txfomer (a Geneformer minimal reimplementaion) performs poorly, and seems to have negligible scaling with increased cell number. In this section, we first show that several implementation details are not the cause of the poor Txfomer scalability. Then, we show that Txfomer representations perform similarly to zero-shot

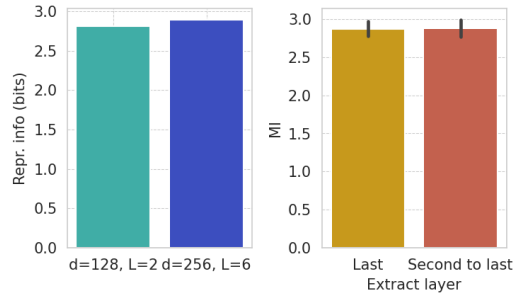


Figure 8: **Reduced scale of Txformer compared to Geneformer does not degrade performance.** (left) Protein representation information of Txformer models of different scale trained on $3 \cdot 10^4$ PBMCs. “L” refers to number of encoder layers, and “d” refers to embedding size in dimensions. (right) Protein representation information of embeddings extracted from different layers of Txformer models trained on $3 \cdot 10^4$ PBMCs. Mean over 2 layer, 128 dimensional embeddings and 6 layer, 256 dimensional embeddings.

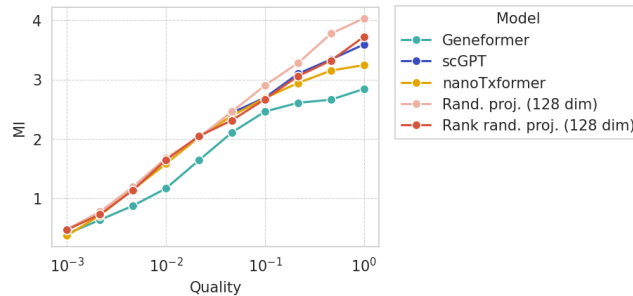


Figure 9: **Txformer performs similarly to zero-shot Geneformer and scGPT.** Protein information probing of zero-shot Geneformer and scGPT, compared to Txformer models trained on full PBMC dataset, and 128-dimensional random projections of expression counts and ranks. Quality refers to count downsampling fraction. scGPT was not stable for downsampling beyond 10^{-2} .

Geneformer and scGPT representations. Finally, we highlight two roots of poor Txformer performance.

A.5.1. POOR TXFORMER PERFORMANCE IS NOT DUE TO DECREASED MODEL SCALE

While Geneformer uses 256 dimensional embeddings with 6 encoder layers, Txformer uses 128 dimensional embeddings with 2 encoder layers. We chose this smaller scale after observing that there were not significant differences between Txformer implementations with varying model sizes, as shown in [Figure X](#).

A.5.2. POOR TXFORMER PERFORMANCE IS NOT DUE TO CHOICE OF EMBEDDING LAYER

While Geneformer (in zero-shot settings) uses embeddings from the second to last transformer encoder layer, Txformer directly uses the last layer. In [Figure X](#), we show that there are not appreciable differences in cell embedding quality between the last two encoder layers of Txformer.

A.5.3. TXFORMER REPRESENTATIONS ARE SIMILAR TO ZERO-SHOT GENEFORMER AND SCGPT EMBEDDINGS

Next, we show that the quality of Txformer representations, as measured by information-theoretic probing, is similar to that of zero-shot Geneformer and scGPT representations of the PBMC CITE-seq dataset across differing data quality. We obtain Geneformer and scGPT representations using the Helical API ([Helical, 2024](#)). We compare their representations to two linear baselines: 128-dimensional random projections of counts, and 128-dimensional random projections of gene expression ranks (modelling information loss in Txformer tokenization).

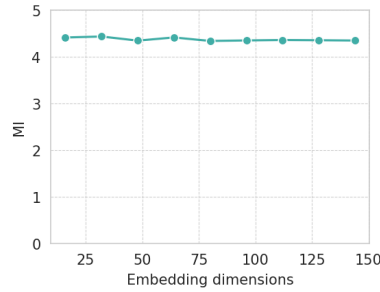


Figure 10: **Increased representation dimensionality does not result in MI estimation artifacts.** Protein information probing of top 16 PCs of full PBMC dataset, where dimensionality is artificially increased by tiling the original 16 dimensions.

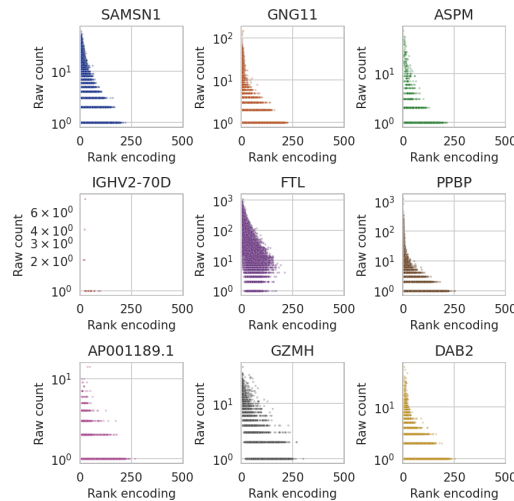


Figure 11: **Rank encoding does not preserve absolute count information.** Rank encoding value compared to absolute expression counts for 9 randomly selected genes in the PBMC CITE-seq dataset.

A.5.4. LOW INFORMATION-PROBE QUALITY IS NOT DUE TO INCREASED EMBEDDING DIMENSIONALITY

One critical difference between Txformer representations and the other studied representations is their dimensionality. Here, we verify that differences in information-probe quality do not arise as a result of dimensionality. We verify this by measuring information probe quality of PCA representations, as they are tiled to artificially increase dimensionality (Fig x). We find that information probe quality remains consistent beyond 128 dimensions, demonstrating that probe quality differences cannot be attributed to dimensionality artifacts.

A.5.5. RANK ENCODING TOKENIZATION LOSES INFORMATION

One clear source of information loss in Txformer (and Geneformer) is during tokenization. Absolute gene expression counts are converted to median normalized expression ranks per gene. While correlated, expression counts and expression ranks are far from equivalent. In Figure X, we visually counts and ranks for 9 randomly selected genes in the PBMC CITE-seq dataset.

Here, we quantify the impact of this information loss in representation quality. We reasoned that if rank encoding is in effect denoising the data rather than degrading useful information, then random projections of rank-encoded data should be equally informative as random projections of absolute counts. We compare the two approaches for the PBMC CITE-seq data and show the results in Figure X. For very noisy data, counts and ranks seem to contain similar amounts of information, but as sensitivity increases, count-based random projections begin to appreciably outperform rank-based random projections. This suggests that for high-quality scRNA-seq data, rank-encoding tokenization will decrease the information that can be

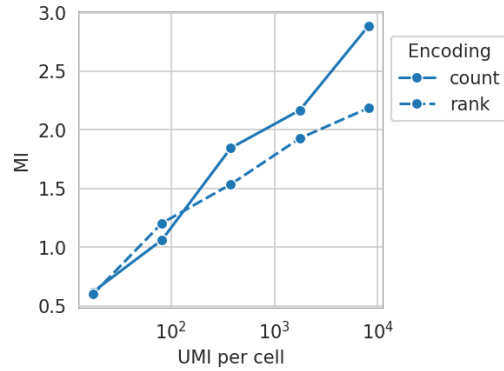


Figure 12: **Rank encoding degrades informativity of random projections.** Protein information of 16 dimensional random projections of gene expression counts compared to cell-wise median-normalized gene expression ranks (equivalent to Geneformer tokenization procedure).

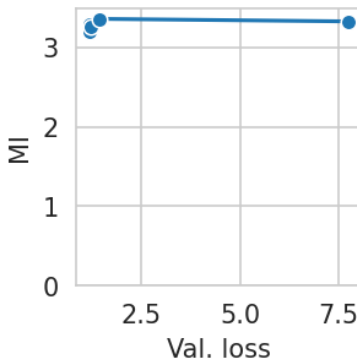


Figure 13: **Improving model loss does not improve Txformer cell embeddings.** Validation loss compared to protein information of Txformer trained on $\sim 10^3$ PBMCs, during 5 epochs of training.

extracted by a representation learning model.

A.5.6. MASKED LANGUAGE MODELLING LOSS IS NOT CORRELATED WITH EMBEDDING QUALITY

The fact that increasing training dataset size does not improve cell embedding quality suggests that the model training objective is not related to cell embedding quality. Here, we concretely test this by measuring information probe quality during training, and comparing representation quality to model loss. Interestingly, we find that representation quality is not correlated with model loss. This indicates that masked language modelling loss for rank-encoding tokenized data can be decreased without learning meaningful mean-pooled embeddings. Perhaps mean-pooling is not the ideal way of extracting cell embeddings from a Geneformer-like model.

A.6. Additional figures

Here we provide visualization of all cellular representation quality scaling law fits in the paper. In Fig. 14, we show all fits of Eq. 1 to cellular representation quality scaling with cell number. In Fig. 15, we show all fits of Eq. 2 to cellular representation quality scaling with UMIs per cell.

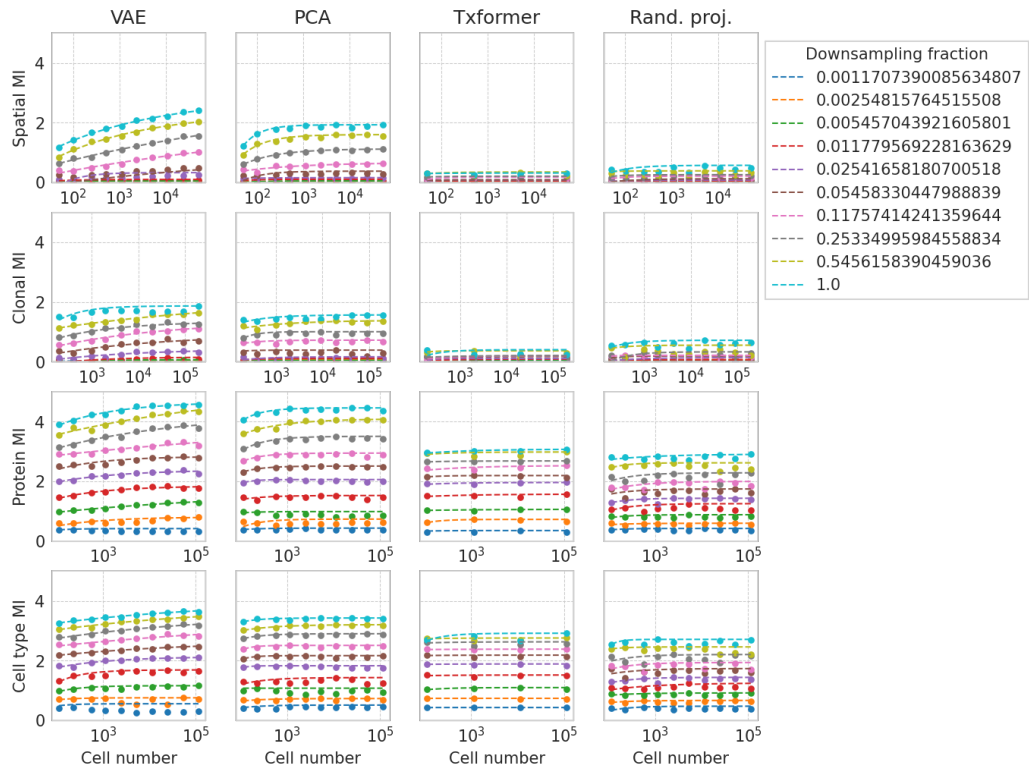


Figure 14: All fits of Eq. 1 to sample number scaling for cellular representation quality with fixed measurement noise.

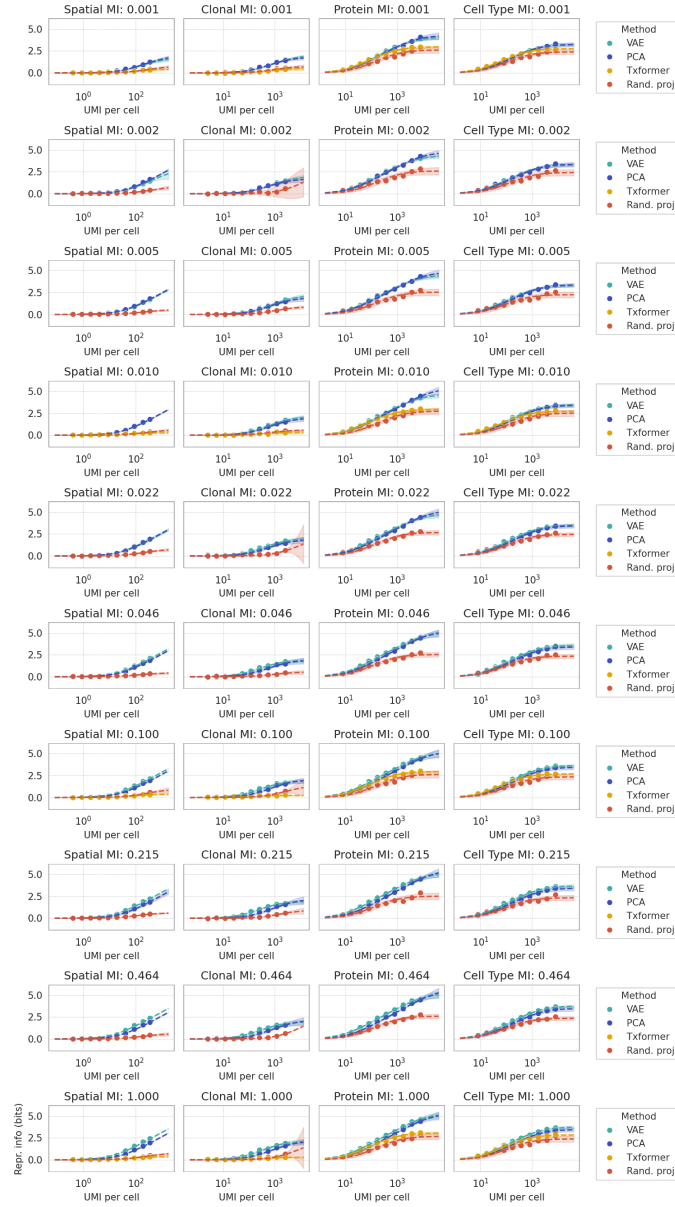


Figure 15: All fits of Eq. 2 to measurement noise scaling for cellular representation quality with fixed dataset size. Shaded region denotes 2σ confidence interval.